High-speed line-field confocal holographic microscope for quantitative phase imaging

Changgeng Liu,[1,5] Sebastian Knitter,[2] Zhilong Cong,[1] Ikbal Sencan,[1] Hui Cao,[2] and Michael A. Choma[1,2,3,4,*]

[1]*Department of Radiology and Biomedical Imaging, Yale School of Medicine, New Haven, Connecticut 06520, USA*
[2]*Department of Applied Physics, Yale University, New Haven, Connecticut 06520, USA*
[3]*Department of Biomedical Engineering, Yale University, New Haven, Connecticut 06520, USA*
[4]*Department of Pediatrics, Yale School of Medicine, New Haven, Connecticut 06520, USA*
[5]*changgeng.liu@yale.edu*
[*]*michael.choma@yale.edu*

Abstract: We present a high-speed and phase-sensitive reflectance line-scanning confocal holographic microscope (LCHM). We achieved rapid confocal imaging using a fast line-scan CCD camera and quantitative phase imaging using off-axis digital holography (DH) on a 1D, line-by-line basis in our prototype experiment. Using a 20 kHz line scan rate, we achieved a frame rate of 20 Hz for 512x512 pixels *en-face* confocal images. We realized coherent holographic detection two different ways. We first present a LCHM using off-axis configuration. By using a microscope objective of a NA 0.65, we achieved axial and lateral resolution of ~3.5 micrometers and ~0.8 micrometers, respectively. We demonstrated surface profile measurement of a phase target at nanometer precision and the digital refocusing of a defocused confocal *en-face* image. Ultrahigh temporal resolution M mode is demonstrated by measuring the vibration of a PZT-actuated mirror driven by a sine wave at 1 kHz. We then report our experimental work on a LCHM using an in-line configuration. In this in-line LCHM, the coherent detection is enabled by moving the reference arm at a constant speed, thereby introducing a Doppler frequency shift that leads to spatial interference fringes along the scanning direction. Lastly, we present a unified formulation that treats off-axis and in-line LCHM in a unified joint spatiotemporal modulation framework and provide a connection between LCHM and the traditional off-axis DH. The presented high-speed LCHM may find applications in optical metrology and biomedical imaging.

OCIS codes: (180.1790) Confocal microscopy; (170.5810) Scanning microscopy.

References and links

1. M. Minsky, "Memoir on inventing scanning confocal microscope," Scanning **10**(4), 128–138 (1988).
2. R. H. Webb, "Confocal optical microscopy," Rep. Prog. Phys. **59**(3), 427–471 (1996).
3. J. B. Pawley, ed., *Handbook of Biological Confocal Microscopy* (Springer, 2006), pp. 381–439.
4. T. R. Corle and G. S. Kino, eds., *Confocal Scanning Optical Microscopy and Related Imaging Systems* (Academic, 1996), pp. 225–275.
5. R. A. Herring, "Confocal scanning laser holography, and an associated microscope: a proposal," Optik (Stuttg.) **105**, 65–68 (1997).
6. P. Jacquemin, R. McLeod, D. Laurin, S. Lai, and R. A. Herring, "Design of a confocal holography microscope for Three-dimensional temperature measurements of fluids in microgravity," Microgravity Sci. Technol. **17**(4), 36–40 (2005).
7. E. Cuche, F. Bevilacqua, and C. Depeursinge, "Digital holography for quantitative phase-contrast imaging," Opt. Lett. **24**(5), 291–293 (1999).
8. M. K. Kim, "Principles and techniques of digital holographic microscopy," SPIE Reviews **1**, 1–50 (2010).
9. A. S. Goy and D. Psaltis, "Digital confocal microscope," Opt. Express **20**(20), 22720–22727 (2012).

#260463 Received 3 Mar 2016; revised 10 Apr 2016; accepted 11 Apr 2016; published 19 Apr 2016

10. A. S. Goy, M. Unser, and D. Psaltis, "Multiple contrast metrics from the measurements of a digital confocal microscope," Biomed. Opt. Express **4**(7), 1091–1103 (2013).
11. M. Schnell, M. J. Perez-Roldan, P. S. Carney, and R. Hillenbrand, "Quantitative confocal phase imaging by synthetic optical holography," Opt. Express **22**(12), 15267–15276 (2014).
12. K. B. Im, S. Han, H. Park, D. Kim, and B. M. Kim, "Simple high-speed confocal line-scanning microscope," Opt. Express **13**(13), 5151–5156 (2005).
13. P. J. Dwyer, C. A. DiMarzio, J. M. Zavislan, W. J. Fox, and M. Rajadhyaksha, "Confocal reflectance theta line scanning microscope for imaging human skin in vivo," Opt. Lett. **31**(7), 942–944 (2006).
14. M. Mujat, R. D. Ferguson, N. Iftimia, and D. X. Hammer, "Compact adaptive optics line scanning ophthalmoscope," Opt. Express **17**(12), 10242–10258 (2009).
15. Y. G. Li, L. Liu, F. Amthor, and X. C. Yao, "High-speed line-scan confocal imaging of stimulus-evoked intrinsic optical signals in the retina," Opt. Lett. **35**(3), 426–428 (2010).
16. L. Mastropasqua and M. Nubile, *Confocal Microscopy of the Cornea* (Slack Incorporated, 2002).
17. C. Liu, S. Marchesini, and M. K. Kim, "Quantitative phase-contrast confocal microscope," Opt. Express **22**(15), 17830–17839 (2014).
18. C. Liu and M. K. Kim, "Digital adaptive optics line-scanning confocal imaging system," J. Biomed. Opt. **20**(11), 111203 (2015).
19. R. K. Wang, "In-vivo full range complex Fourier domain optical coherence tomography," Appl. Phys. Lett. **90**(5), 054103 (2007).
20. R. N. Bryan, *Introduction to the Science of Medical Imaging* (Cambridge University Press, 2009).
21. S. T. Thurman and J. R. Fienup, "Phase-error correction in digital holography," J. Opt. Soc. Am. A **25**(4), 983–994 (2008).
22. S. G. Adie, B. W. Graf, A. Ahmad, P. S. Carney, and S. A. Boppart, "Computational adaptive optics for broadband optical interferometric tomography of biological tissue," Proc. Natl. Acad. Sci. U.S.A. **109**(19), 7175–7180 (2012).
23. B. Redding, Y. Bromberg, M. A. Choma, and H. Cao, "Full-field interferometric confocal microscopy using a VCSEL array," Opt. Lett. **39**(15), 4446–4449 (2014).
24. Y. Choi, P. Hosseini, W. Choi, R. R. Dasari, P. T. C. So, and Z. Yaqoob, "Dynamic speckle illumination wide-field reflection phase microscopy," Opt. Lett. **39**(20), 6062–6065 (2014).
25. M. G. Somekh, C. W. See, and J. Goh, "Wide field amplitude and phase confocal microscope with speckle illumination," Opt. Commun. **174**(1-4), 75–80 (2000).

1. Introduction

Since its introduction in the mid-1950s [1], point-scanning confocal microscopy (PCM) has found wide applications in industrial inspection, biology and medicine thanks to its capability of achieving high-resolution, high-contrast images and true optical sectioning [2–4]. Driven by the needs of semiconductor metrology, interference methods have been applied in PCM to achieve qualitative or quantitative phase information of the device surface by use of differential interference phase-contrast method, electro-optical modulation or optical heterodyne interferometry [4]. More recently, holography was integrated into a confocal transmission microscope to study fluids under microgravity [5,6]. In this original confocal holographic microscope, the object is raster scanned point by point, and each point is recorded by a 1D hologram with a line-scan camera. Due to the complicated optical system and slow acquisition, it is hard to find applications in other fields. Digital holography (DH) as an emerging imaging modality has found wide applications in optical metrology, biology and medicine thanks to its quantitative phase imaging capability by a quite simple optical and electronic operation [7,8]. A digital confocal microscope (DCM) was proposed by use of wide field off-axis DH in 2012 [9] and quantitative phase imaging of biological samples were reported in 2013 [10]. DCM has a very simple optical system but imposes a heavy computational burden to record and reconstruct one *en-face* confocal image, because each object point is recorded in a 2D off-axis digital hologram. Therefore it is limited to static samples. In 2014, synthetic optical holography (SOH) was proposed to achieve quantitative confocal phase imaging by moving a reference mirror to introduce a spatial frequency carrier [11]. SOH realized one single-shot hologram for one *en-face* confocal image thereby reducing the data flow by 6 orders of magnitude compared to DCM. The speed of the reported SOH is still limited to ~0.1 frame per second due to the stage scanning configuration. It is promising to find more applications if the speed can be improved to tens frames per second. Instead of working with PCM using the above-mentioned phase-sensitive techniques, there has been

#260463 Received 3 Mar 2016; revised 10 Apr 2016; accepted 11 Apr 2016; published 19 Apr 2016

significant interest in line-scanning confocal microscopy (LCM) because it has a simpler optical system and achieves faster data acquisition while maintaining comparable confocal imaging compared to PCM [12–16]. Previous work has demonstrated a quantitative phase-contrast confocal imaging technique by combining DH with a traditional line-scanning confocal microscope [17,18]. In this technique, the line fields are recorded by 2D holograms and reconstructed to achieve *en-face* confocal intensity and phase images. However in the previous embodiments, the speed is limited by the fact that ~1000 2D holograms are needed to reconstruct one *en-face* confocal image and strong phase jitters are introduced due to stage scanning.

To overcome prior limitations, in this paper, we report a high-speed line-scanning confocal holographic microscope (LCHM) which adopts beam scanning and a high-speed line-scan CCD camera. Line fields from the sample are not recorded by 2D off-axis holograms but by 1D off-axis line-by-line holograms. Using a 20 kHz line scan rate, we achieved a frame rate of 20 Hz for 512x512 pixels *en face* confocal images. By using a microscope objective of a NA 0.65, we achieved an axial and lateral resolution of ~3.5 micrometers and ~0.8 micrometers, respectively. By z-stack imaging of a custom silicon target with a stepped structure, we confirmed that the axial sectioning of the LCHM is similar to that of a traditional line-scanning confocal microscope. Using a custom axial height phantom fabricated using chrome deposition, we demonstrated variations in phase corresponding to heights in the ~100 nm range with a contrast-to-noise ratio of ~31 dB. The phase aberration of the optical system can be recorded and removed in the LCHM, which was demonstrated by digitally refocusing of an out-of-focus holographic image. Ultrahigh temporal resolution M-mode is demonstrated by measuring the vibration of a PZT-actuated mirror driven by a sine wave at 1000Hz. Coherent detection in the LCHM can also be realized in a in-line optical configuration by moving the reference beam as demonstrated in SOH and spectral-domain optical coherence tomography [11,19]. Doppler frequency shift due to the moving reference beam can introduce the spatial fringes along the scanning direction. The fringe density can be flexibly designed by varying the speed at which the reference beam moves, and diffraction-limited lateral resolution can be achieved without affecting the field of view, while the precision of the phase map remains unchanged compared to the off-axis LCHM. Combining off-axis configuration and moving refence beams, the fringe orientation can be adjusted by setting different speed at which the reference beam moves.We will present a general formulation to describe the basic principle of this mixed experimental scheme and our experimental validation.

This paper is organized as follows. In Section 2, The optical apparatus, the principle and experimental demonstrations of the LCHM using traditional off-axis configuration are presented. The principle and experimental realization of the LCHM using in-line configuration and a moving reference beam will be given in Section 3. In Section 4, a general mathematical description of the LCHMs using traditional off-axis and a moving reference beam will be given. Also, an experimental validation will be presented in this section. The final conclusions will be given in Section 5.

#260463 Received 3 Mar 2016; revised 10 Apr 2016; accepted 11 Apr 2016; published 19 Apr 2016

2. Off-axis line-scanning confocal holographic microscope

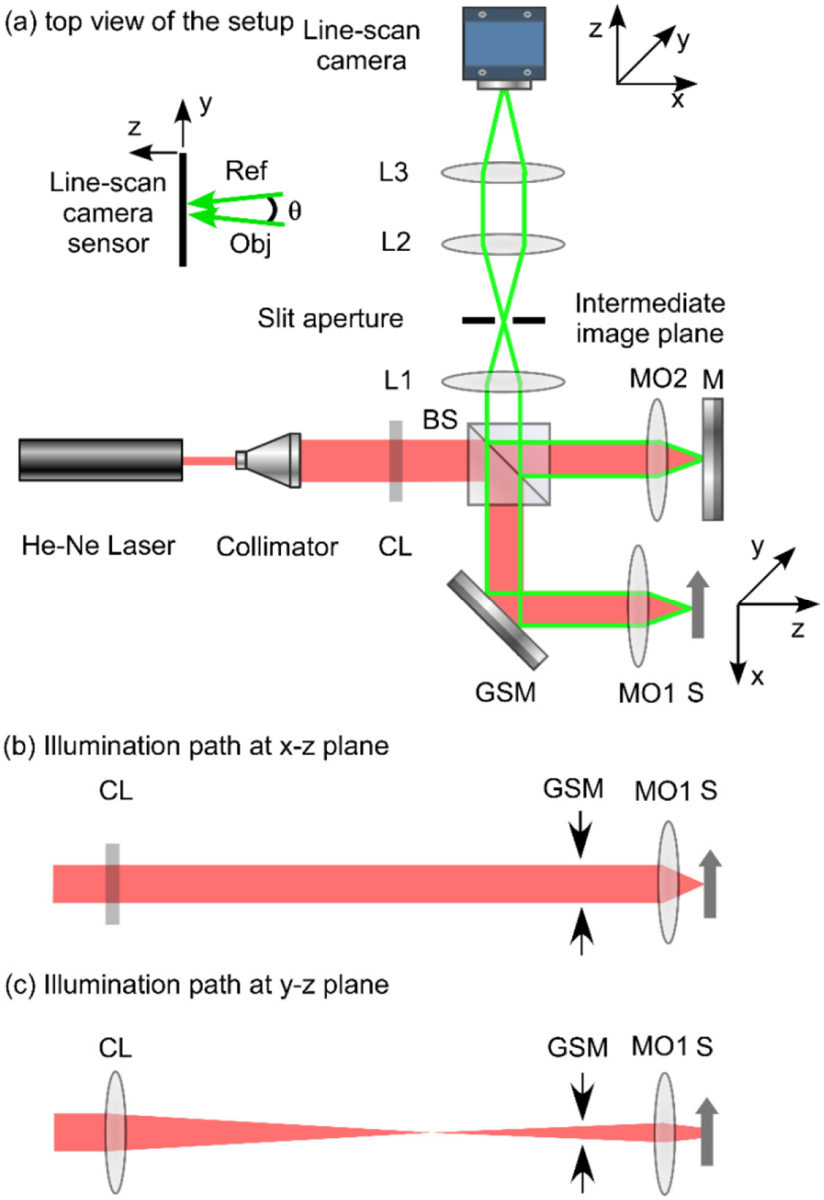

Fig. 1. Schematic diagram of optical apparatus of the off-axis LCHM. (a) Top view (x-z plane or the optical tabletop plane) of the optical layout. CL: cylindrical lens with a focal length of 100mm. GSM: Galvanometer scanning mirror. MO1 and MO2: Microscope objectives (NA 0.65, 65 ×). L1-L3: regular singlet lens. Focal lengths are 300mm, 35mm, and 125mm respectively. (b) Illumination path at x-z plane. (c) Illumination path at y-z plane.

2.1 Experimental setup

The optical system is depicted in Fig. 1. In contrast to the previous optical systems that employ a Mach-Zehder interferometer, and stage-scanning configuration with a 2D CCD [17], the optical apparatus in Fig. 1 adopts a Michelson type of interferometer, and beam-scanning configuration with a high speed line-scan CCD. Figure 1(a) shows the top view of

#260463 Received 3 Mar 2016; revised 10 Apr 2016; accepted 11 Apr 2016; published 19 Apr 2016

the optical layout. A He-Ne laser with an output power of ~1.2 mW and the central wavelength λ of 632.8 nm is used as the light source. A cylindrical lens CL with a focal length of 100mm is employed to deliver a line focus oriented along y direction at the back focal plane of the microscope objective MO1 with a NA 0.65 and an effective focal length 4.5 mm where the sample S is placed. In the coordinate system in Fig. 1(a), z represents the direction of optical axis in both illumination and imaging paths, x-z plane is parallel with the optical tabletop, and y direction is perpendicular to the optical tabletop. The line illuminations at the x-z plane (optical tabletop plane) and y-z plane through the cylindrical lens CL and the microscope objective MO1 are detailed in Figs. 1(b) and 1(c) respectively. The length of line focus at the sample is ~110 μm. The intermediate image plane of the sample plane is at the back focal plane of the lens L1 (focal length: 300 mm), which results in a magnification of ~66.7 between the intermediate image over the object. A relay optics composed of the lens L2 (focal length: 35mm) and the lens L3 (focal length: 125 mm) magnifies the intermediate image by a factor of ~3.3 onto the line-scan camera. Therefore the total magnification of this imaging system is ~222. We put a slit aperture at the intermediate image plane which is used as the object of the relay optics L2 and L3 to facilitate the alignment and reject the noisy reflections. The line-scan CCD camera (AVIIVA EM2, Model: EV71YEM2CL1014-BA9) is put at the final image plane of the object, which has 1024 pixels with a pixel pitch of 14 μm (y direction) by 28 μm (x direction) and a maximum line rate of 70 kHz. The sample is scanned along the x direction by use of a galvanometer scanning mirror GSM. The synchronization between the image acquisition and the GSM scanning is described as follows. The line-scan camera is controlled by a desktop computer through a frame grabber (BitFlow Inc. B-NEO-PCE-CLB) which can be programmed to send a TTL signal at the beginning of each frame. This TTL signal is used as the trigger signal for the function generator (Stanford Research Systems, DS345) to generate one cycle of saw tooth wave. This saw tooth wave is then sent to the galvanometer driver through a BNC cable to scan the GSM. To perform the 1D off-axis DH, a Michelson-type interferometer is built by introducing a reference arm with a matching microscope objective MO2 of the same parameters as MO1 and a mirror placed at the back focal plane of MO2. The off-axis angle between the reference and object beams θ as shown in Fig. 1(a) was introduced by slightly tilting the beam splitter BS at the y-z plane.

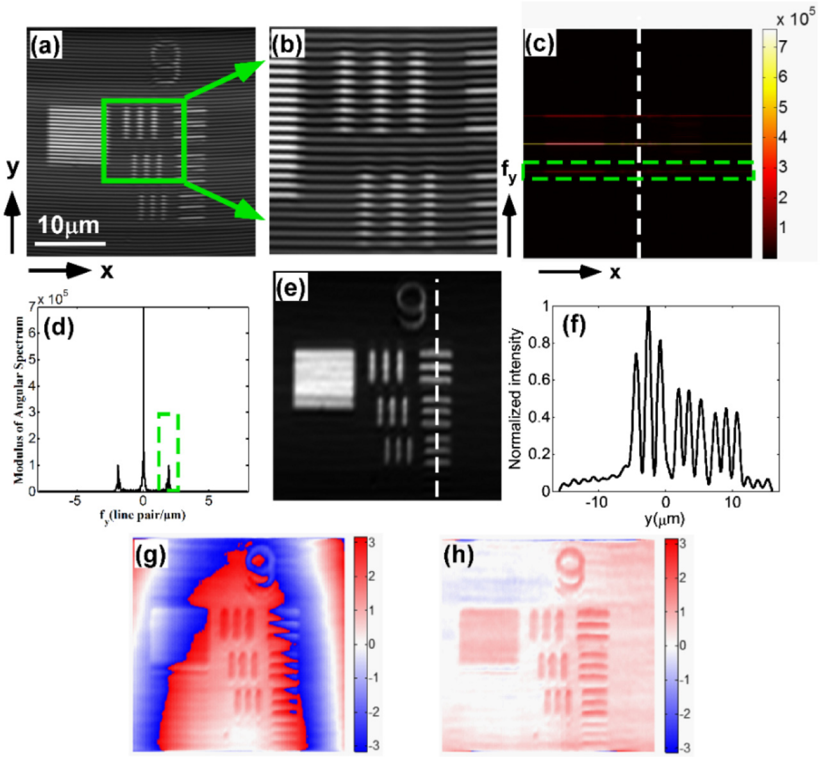

Fig. 2. Demonstration of the principle of operation and data processing. (a) Digital hologram of 512 line holograms. (b) Magnified view of the region in (a) highlighted by the green square. (c) AS of (a) by taking 1D FT of (a) along y direction. (d) Profile along the dashed white line in (c). (e) Reconstructed intensity. (f) Profile along dashed white line in (e). (g) Reconstructed phase map (in radians) from the hologram (a). (h) The corrected phase map.

2.2 Data processing

The intensity of a 1D off-axis hologram recorded by the camera at a given x position can be expressed as

$$\begin{aligned} H(x,y) = {} & |O(x,y)|^2 + |R(x,y)|^2 \\ & +2|O(x,y)||R(x,y)|\cos[2\pi f_{yc} y + \phi(x,y) + \phi_a(x,y)] \end{aligned} \tag{1}$$

where O(x,y) and R(x,y) represent the object and reference fields at the camera plane respectively. The cosine term represents the interference between them. f_{yc} is the carrier spatial frequency that is related to the off-axis angle θ by $f_{yc} = \frac{\sin(\theta)}{\lambda}$, where λ is the wavelength of the light source [8]. In this experiment, θ is ~0.32 degrees which corresponds to the f_{yc} of ~8.8 line pairs/mm (in image space) or ~1.93 line pairs/μm (in object space). ϕ(x, y) represents the phase variation introduced by the sample assuming the mirror itself does not introduce phase variation. $\phi_a(x, y)$ consists of the aberration introduced by the optical system, and the phase jitter caused by the GSM. The aberration due to the optical system can be removed by an empty hologram as the wide field off-axis DH does [8]. The phase jitter can be removed by using a correction algorithm which has been detailed in [17]. To retrieve the complex signal from the line hologram, we need take 1D Fourier transform (FT) of Eq. (1) along y direction. The resulting spatial angular spectrum (AS) contains zeroth-order term, image and twin-image terms as in the wide field off-axis DH [8]. Either of the latter two

Received 3 Mar 2016; revised 10 Apr 2016; accepted 11 Apr 2016; published 19 Apr 2016

terms can be filtered out, shifted to the center of the spatial AS and inversely Fourier transformed to reconstruct the complex signal of object field. This process is demonstrated by using the experimental data on a high-resolution United States Air Forces (USAF) test chart (Edmund Optics, #58-198) in Fig. 2. Figure 2(a) shows a 2D hologram which is composed of 512 line holograms. Each of this line hologram can be modelled by Eq. (1) at given x position. The magnified view of the region within the green square in Fig. 2(a) is shown in Fig. 2(b). The spatial AS is shown in Fig. 2(c) by taking 1D FT of Fig. 2(a) along y direction. Region highlighted by the dashed green rectangle is the twin-image term. The profile along the dashed line in Fig. 2(c) is shown in Fig. 2(d) where the spatial frequency is calculated in object space. By windowing the twin-image term indicated by dashed green box in Fig. 2(d), shifting it to the center, and taking 1D inverse FT of it, we are able to obtain complex signal of this line field. The full-field object field is the reconstructed this way line by line. The reconstructed intensity image is shown in Fig. 2(e). The profile along dashed white line in Fig. 2(e) is shown in Fig. 2(f). The width of the smallest bar is 0.78μm which can be clearly resolved. Therefore, it can be claimed that the lateral resolution of this imaging system is ~0.8 μm. The reconstructed phase map (in radians) is shown in Fig. 2(g), which contains the phase aberration $\phi_a(x, y)$. Note that the phase jitters in LCHM are much weaker compared to those from the stage-scanning case [17] owing to high-speed scanning. We then use an empty hologram [8] and phase jitter correction algorithm [17] in a sequence to remove these two phase terms. The resulting corrected map is shown as in Fig. 2(h).

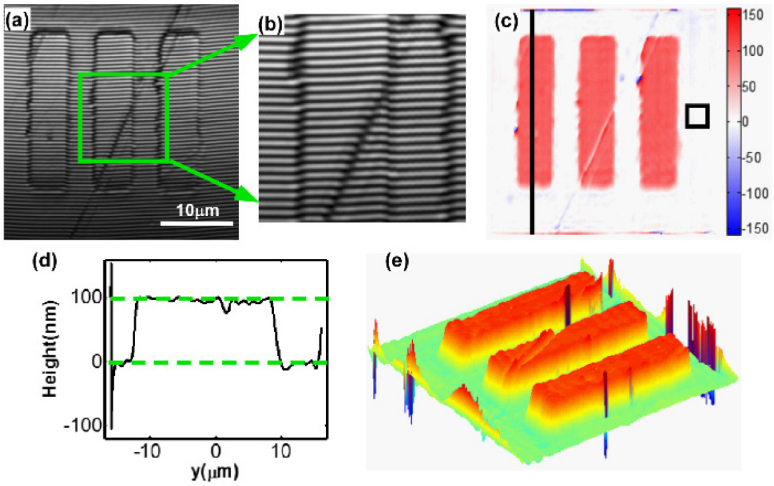

Fig. 3. Quantitative phase imaging of a phase target. (a) Raw hologram. (b) Magnified view of the region in (a) indicated by the green square. (c) The surface height map of the phase target after correction. (d) The profile along solid black line in (c). (e) 3D rendering of (c).

2.3 Confocal phase map

The difference of phase shifts between the air-glass and air-chrome interfaces makes it difficult to calibrate the confocal phase measurements. To solve this problem, the quantitative phase imaging was evaluated by use of a custom phase target through chrome depositions.The height of the bars are around 100nm verified by an atomic force microscope [17]. Figure 3(a) shows the raw hologram and the detailed view in the green square is shown in Fig. 3(b). The height map (in nm) calculated from reconstructed phase map by $\frac{\phi(x,y)}{4\pi}\lambda$ is shown in Fig. 3(c). The profile along the solid black line is shown in Fig. 3(d). Height difference between the two green dashed lines in Fig. 4(d) as 98.6nm. The uncertainty is evaluated by calculating the standard deviation of the empty region within the black box in Fig. 3(c) is 2.8nm. Therefore, the contrast-noise-ratio (CNR) defined by $20\log_{10}(\frac{H}{S})$ is calculated as 31dB, where H represents the absolute value of the height difference between the top and the base of the bars, and S denotes the height standard deviation in the flat region of the height map [20]. Figure 3(e) shows the 3D rendering of the height map in Fig. 3(c).

2.4 Axial sectioning

The axial sectioning was tested by moving a mirror at the sample plane in Fig. 1(a) through the focal plane and evaluating the total image intensity with respect to the distance away from the focal plane. The axial response curve of LCHM is the dark solid line shown in Fig. 4(a) which has a full width at half maximum (FWHM) ~3.5 µm. As a comparison, the axial response curve from LCM as shown by the dotted blue line in Fig. 4(a) has a FWHM ~3.6 µm, which means the LCHM does not affect the axial sectioning compared to LCM. To demonstrate the axial sectioning capability, we apply the LCHM to a two stepped silicon wafer with a height ~22 µm, verified by an optical profilometer. Figure 4(b) shows the *en-face* images at z = 0 µm. The corresponding phase map is shown in Fig. 4(c). Figure 4(d) shows the *en-face* images at z = 22 µm. Its corresponding phase map is shown in Fig. 4(e). Note that the phase maps only within the green rectangle in Figs. 4(c) and 4(e) are meaningful. In other regions, the phase is not well defined. Figure 4(f) shows the y-z section at the x position indicated by the dashed line in Fig. 4(d). The difference in z corresponding to the maximum values at the two steps is measured as ~23 µm at this x position.

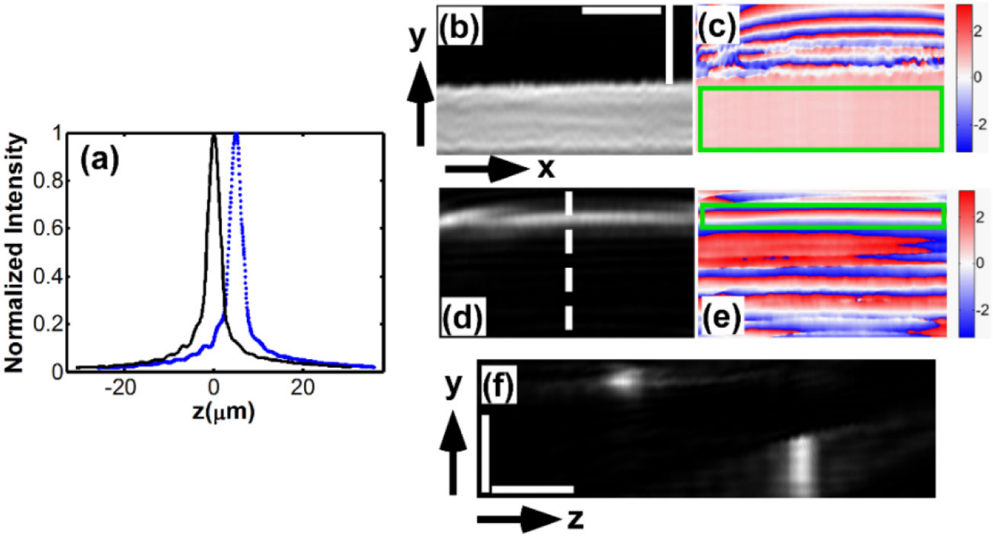

Fig. 4. Axial resolution measurement and experimental demonstration using a silicon wafer. (a) Axial responses with respect to the distance away from the focal plane from LCHM and LCM. (b) *En-face* intensity image at the top layer from LCHM. (c) *En-face* phase map at the top layer from LCHM. (d) *En-face* intensity image at the bottom layer, and (e) *En-face* phase map at the top layer. (f) y-z section along the x position indicated by the dashed line in (d). Scale bars: 10 µm.

2.5 Digital refocusing

We then demonstrate that LCHM is able to digitally refocus the defocused en-face image. Figures 5(a) and 5(b) are the intensity and phase of a defocused image from LCHM. We then numerically propagate it by a distance of ~110 mm in the image space, which corresponds to a distance of ~2.1μm in object space to the focal plane by use of angular spectrum method [8]. For the angular spectrum method, the complex field O(x, y, d) at a diffraction distance d is computed from the field O(x, y, 0) at the CCD plane by $O(x,y,d) = IFT2\{FT2[O(x,y,0)]\exp[\frac{j2\pi d}{\lambda}\sqrt{1-(\lambda f_x)^2-(\lambda f_y)^2}]\}$, where FT2 and IFT2 denote 2D Fourier transform and 2D inverse Fourier transform respectively, and f_x and f_y represent the coordinates in the spatial frequency domain of O(x, y, 0), and j means $\sqrt{-1}$.The intensity and phase of the refocused image are shown in Figs. 5(c) and (d). Note that phase jitter correction method [17] was used to reduce the artefacts caused by the propagation of the phase jitter into the refocused image before the numerical propagation. The phase jitter correction procedure has removed part of the phase aberration $\phi_a(x, y)$, which depends only on x. That can explain why the phase map in Fig. 5(d) appears different that from Fig. 5(b).

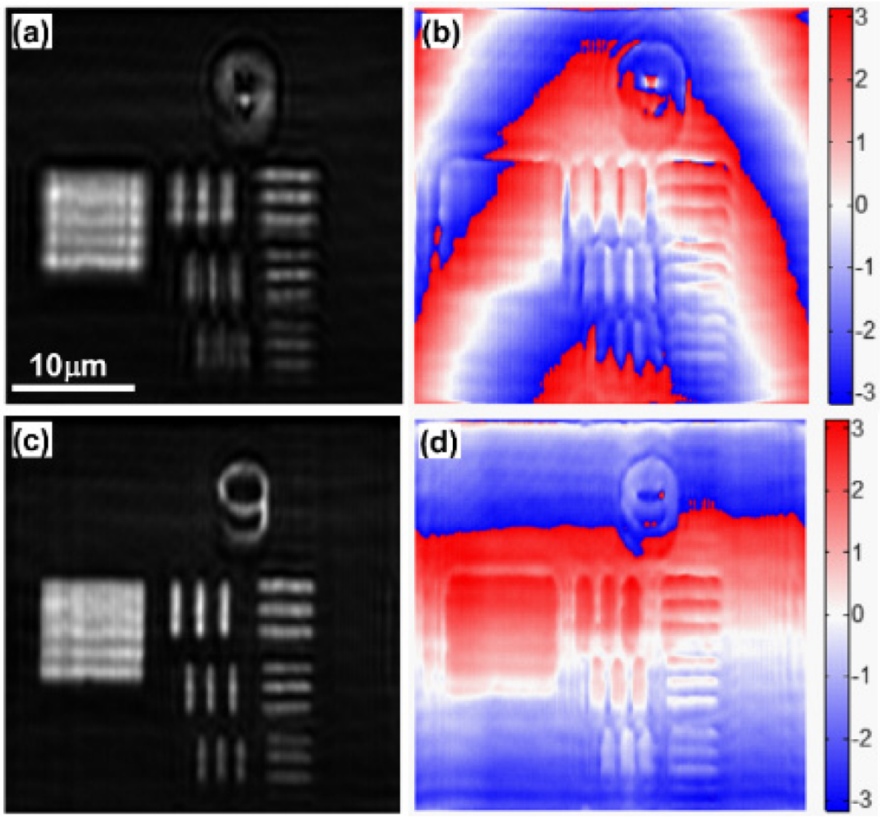

Fig. 5. Demonstration of digital refocusing by LCHM. (a), and (b) are the intensity and phase of the defocused field respectively. (c), and (d) are the refocused fields by numerically propagating the field of (a) and (b) by a distance of 110mm in image space.

2.6 High-frequency vibration measurement by M-mode

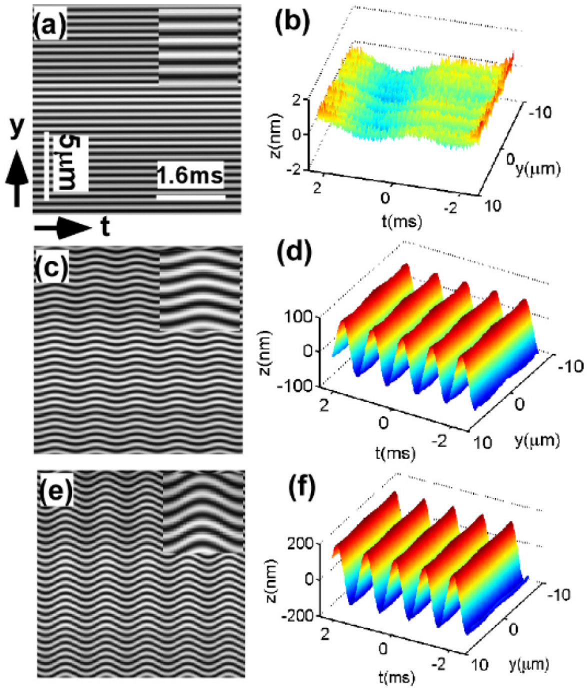

Fig. 6. Vibration measurement by LCHM. (a) Hologram at y-t plane at V = 0 Volts (Inset × 2). (b) z(y, t) from (a). (c) Hologram at V = 2.5 Volts. (d) z(y, t) from (b). (e) Hologram at V = 5 Volts. (f) z(y, t) from (e).

LCHM can work in both frame-by-frame mode as above mentioned and in line-by-line or M mode. In line-by-line mode, the GSM is fixed at the specified scanning angle while taking the line holograms at ultrahigh temporal resolution. We demonstrate this mode by measuring the displacement z(y, t) of a mirror along the optical axis, where t means time. This mirror is placed at the sample plane and mounted onto a PZT actuator (Thorlabs, AE0203DOF) driven by a sine wave at 1000 Hz which is provided by a function generator. In this experiment, we set the line rate of the camera to be 50 kHz. The holograms and reconstructed z(y, t) maps at different amplitudes V of the driving wave are shown in Fig. 6. Figure 6(a) shows the y-t hologram at V = 0 Volts, which contains 256 line holograms at 256 different temporal instants at a step of 20 μs. The fringes along temporal axis are quite straight, which means the phase variation is very small along temporal axis. The corresponding z(y, t) distribution reconstructed is shown in Fig. 6(b). The standard deviation of z(y, t) is ~0.4 nm. This z(y, t) distribution can be attributed to the vibration inherent in the optical system during this temporal interval. Figure 6(c) shows the y-t hologram at V = 2.5 Volts, where the fringes along y direction are modulated in a sine waveform. The resulting z(y, t) distribution is shown in Fig. 6(d). The average amplitude of z(y, t) at different y positions are ~82.9 nm. Figure 6(e) shows the y-t hologram at V = 5.0 Volts, where the fringes along y direction are also modulated in a sine waveform with a stronger strength compared to Fig. 6(c). The resulting z(y, t) distribution is shown in Fig. 6(f). The average amplitude of z(y, t) at different y positions are ~165.2 nm, which is approximately twice that compared to the vibration at V = 2.5 Volts.

#260463 Received 3 Mar 2016; revised 10 Apr 2016; accepted 11 Apr 2016; published 19 Apr 2016

3. Line-scanning confocal holographic microscope using in-line configuration

In Section 2, a LCHM using traditional off-axis configuration is presented, where each off-axis 1D holograms are decoded and combined to achieve the *en face* complex field. In this section, we present a different way to achieve the off-axis hologram. Instead of using off-axis optical configuration, in-line optical configuration is employed. The spatial fringes are generated by use of Doppler frequency shift introduced by moving a reference beam. The principle, experimental demonstrations and a comparison with the traditional off-axis LCHM described in section 2 will be presented in this section.

3.1 Principle of operation

The optical system of the LCHM with in-line configuration is similar to the off-axis LCHM. The difference is we adjust the off-axis angle θ close to zero degree and we mount both MO2 and the mirror M in Fig. 1(a) onto a motorized stage and moving them at a specified speed. The resulting digital hologram can be expressed as follows,

$$\begin{aligned} H(t,y) &= \left|R(y)\exp(-\mathrm{j}2\pi f_{Tc}t) + O(t,y)\right|^2 \\ &= \left|R(y)\right|^2 + \left|O(t,y)\right|^2 + 2\left|R(\mathrm{y})\right|\left|O(t,y)\right|\cos[2\pi f_{Tc}t + \varphi(t,y) + \varphi_b(t,y)] \end{aligned} \tag{2}$$

where t is the time, y the coordinate along the parallel detection. $\varphi(t,y)$ is the phase information of the object, $\varphi_b(t,y)$ represents aberration term which is composed of the aberration of the optical system, and the jitter from the GSM, motorized stage and the speed variation from the reference beam. f_{Tc} means the temporal carrier frequency which is the Doppler shift introduced by the moving reference beam, which can be expressed as

$$f_{Tc} = \frac{2v_R}{c} f_0 \tag{3}$$

where v_R is the speed of the reference arm, c is the speed of light in the vacuum, f_0 is the central frequency of the light source. To relate the temporal hologram to a more familiar form of spatial hologram, we can rewrite the temporal hologram into a spatial hologram along scanning direction or x direction by the relationship

$$x = v_x t \tag{4}$$

where v_x is the speed at which the illumination line field moves on the sample along x direction. Then the hologram can be expressed as

$$\begin{aligned} H(x,y) &= \left|R(y)\exp(-\mathrm{j}2\pi f_{xc}x) + O(x,y)\right|^2 \\ &= \left|R(y)\right|^2 + \left|O(x,y)\right|^2 + 2\left|R(y)\right|\left|O(x,y)\right|\cos[2\pi f_{xc}x + \varphi(x,y) + \varphi_b(x,y)] \end{aligned} \tag{5}$$

where

$$f_{xc} = \frac{f_{Tc}}{v_x} = \frac{2v_R}{v_x c} f_0 \tag{6}$$

The experimental parameters are set as follows. We set the line period of the line-scan camera to 50 microseconds. The fringe density along x direction is designed as 0.25 line pairs/pixel or 3.96 line pairs/μm. From Eq. (2), we can get f_{Tc} = 5000 Hz. Using Eq. (2), the speed of the stage can be calculated as v_R = 1582 μm/s.The speed v_x can be given by v_x = dx/dt = (0.0631 μm/50 μs) = 1262 μm/s. According to Eq. (6), f_{xc} is calculated as 3.96 line pairs/μm which is used as the filter center to reconstruct the complex signal from the line holograms.

#260463 Received 3 Mar 2016; revised 10 Apr 2016; accepted 11 Apr 2016; published 19 Apr 2016

3.2 Experimental demonstration

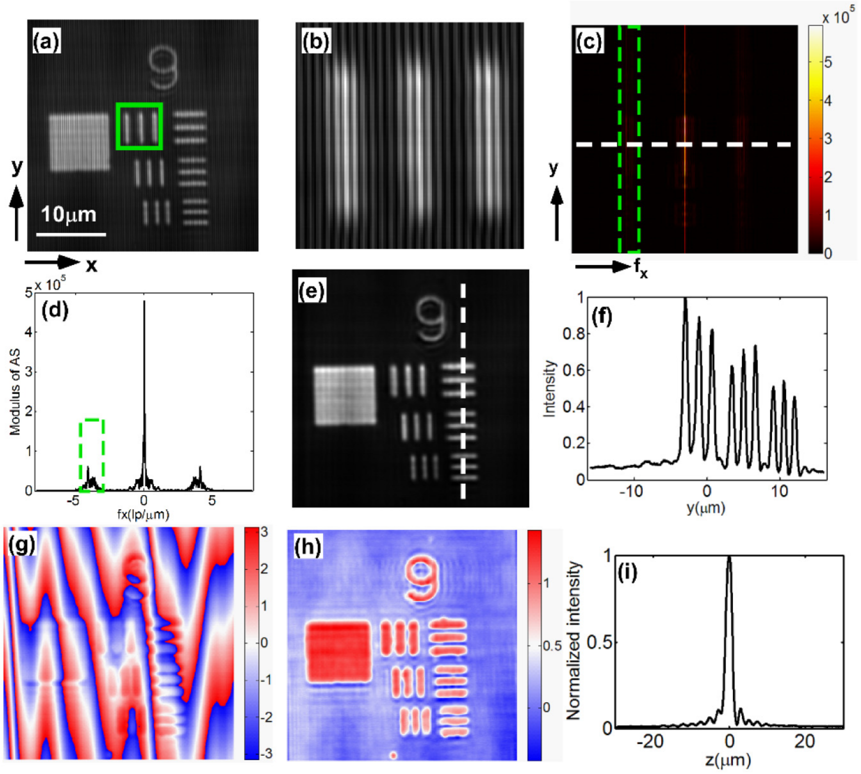

Fig. 7. Demonstration of in line LCHM. (a) hologram. (b) magnified view of the region bounded by the green square in (a). (c) AS. (d) Profile along white dashed line in (c). (e) Reconstructed intensity. (f) profile along the white dashed line in (e). (g) original phase map. (h) corrected phase map. (i) axial response with respect to the distance away from the focal plane.

The experimental results for the in-line LCHM are shown in Fig. 7. The digital hologram is shown in Fig. 7(a). The magnified view of the region bounded by the green square in Fig. 7(a) is shown in Fig. 7(b) we can see the vertical straight fringes due to the sample scanning and the movement of the reference beam. The fringe density is 0.25 cycles/pixel as we have designed. We then take 1D FT along x direction and obtain the 1D AS as shown in Fig. 7(c), where the twin image term is highlighted by the dashed green rectangle. The profile along the white dashed line in Fig. 7(c) is shown in Fig. 7(d). Because the three terms in AS domain are well separated, we are allowed to apply a filter with a width of the cutoff spatial frequency of the optical system. Therefore the reconstructed image is diffraction-limited. The reconstructed intensity image is shown in Fig. 7(e), where the smallest feature is well resolved. The corresponding profile along the dashed white line is shown in Fig. 6(f). Compared to the intensity from off-axis LCHM, the intensity image from in-line LCHM is apparently sharper due to a larger filter size in AS domain. The original phase map is shown in Fig. 7(g) which shows stronger phase aberration compared to the off-axis LCHM because of the speed variation of the motorized stage. To remove the phase aberration, we first use the phase jitter correction algorithm to correct the phase aberration which depends only on x [17]. we found that after this operation the stronger phase variation due to the speed variation of the motorized stage is completely removed. The residual phase aberration is a linear term plus a quadratic term along y direction. We then apply least square fitting procedure to remove it. After phase aberration correction, the corrected phase map is shown in Fig. 7(h). It is worth

#260463 Received 3 Mar 2016; revised 10 Apr 2016; accepted 11 Apr 2016; published 19 Apr 2016

noting that due to the moving reference beam, the phase aberration correction using an empty hologram as employed in off-axis LCHM becomes ineffective. It becomes necessary to apply numerical methods to remove the residual phase aberration arising from the optical system. Using the same phase target in off-axis LCHM, the height difference of the profile is measured as 100.2 nm with a uncertainty of 2.5nm, which corresponds to a contrast to noise ratio of ~32 dB. Although stronger phase aberration exists in the original phase map, the corrected phase map does not show stronger phase uncertainty compared to off-axis LCHM. Using in-line configuration, the off-axis aberration can be removed compared to the off-axis LCHM, that will improve the axial sectioning which is more sensitive to the optical aberration than the lateral resolution. The axial response curve from in-line LCHM with the reference beam blocked is shown in Fig. 7(i) which has a FWHM of ~2.0 μm compared to the ~3.5μm from off-axis LCHM. The mechanical vibration of the reference arm leads to variation of the relative position between the mirror M and MO2, which results in the intensity variation of the reference beam at the camera plane. This intensity variation prevents an accurate measurement of axial sectioning using holographic in-line LCHM. However, holographic process using He-Ne laser does not affect the axial sectioning capability as we have demonstrated in off-axis case. Therefore, it is quite reasonable to claim this axial resolution of this in-line LCHM is ~2.0μm. It is worth pointing out that the phase variation from the moving reference beam makes it difficult to retrieve the phase information from the line-by-line or M Mode.

4. Joint spatiotemporal phase modulation for coherent holographic detection: a unified approach to both off-axis and in-line holography

In this section, we present joint spatiotemporal phase modulation for coherent holographic detection. This approach simultaneously utilizes both off-axis and in-line approaches. We first present a unified description for off-axis LCHM as described in Section 2 and in-line LCHM with a moving reference beam as depicted in Section 3. We then demonstrate that by combining off-axis configuration and a moving reference beam, we are able to change the fringes orientation as off-axis wide-field DH can. The digital hologram can be written in 2D form as follows,

$$\begin{aligned} H(x,y) &= \left|R(x,y)\exp(-j2\pi f_{xc}x)+O(x,y)\right|^2 \\ &= \left|R(x,y)\right|^2+\left|O(x,y)\right|^2+2\left|R(x,y)\right|\left|O(x,y)\right|\cos[2\pi f_{xc}x+2\pi f_{yc}y+\varphi(x,y)+\varphi_c(x,y)] \end{aligned} \quad (7)$$

Where f_{xc} the spatial carrier frequency along x direction as described in Eqs. (5) and (6), f_{yc} is the spatial carrier frequency along y direction as described in Eq. (1). $\varphi(x,\mathrm{y})$ is the phase information of the object, $\varphi_c(x,\mathrm{y})$ represents aberration term which consists of the aberration of the optical system, and the phase jitter caused by the GSM, motorized stage and the speed variation of the reference beam. When $f_{xc} = 0$ or the reference beam is static, Eq. (7) reduces as Eq. (1) for off-axis LCHM. When $f_{yc} = 0$, Eq. (7) becomes the same as the Eq. (5) for in-line LCHM with a moving reference beam. Therefore, if we treat the digital hologram as 2D hologram as wide-field DH, the off-axis LCHM and In-line LCHM are the special case of Eq. (7). The reconstructed images of off-axis and in-line LCHM using 2D data processing as wide-field DH are the same as the 1D line-by-line processing as we have described, because 2D FT or inverse FT are basically two 1D FT or inverse FT in a sequence. Therefore, for these two special cases, 2D processing just increases one 1D FT and 1D inverse FT operations. When we combine off-axis configuration with a moving reference arm, Eq. (7) becomes necessary to describe the experimental result. In the following experiment, we set the off-axis angle θ to be ~0.25degree, which is too small to realize the separation between the image term and the zero term if the reference beam is not moving. The corresponding hologram is shown in Fig. 8(a). The 2D AS which is obtained by taking 2D FT of the

#260463 Received 3 Mar 2016; revised 10 Apr 2016; accepted 11 Apr 2016; published 19 Apr 2016

hologram in Fig. 8(a) is shown in Fig. 8(b) in logarithmic intensity scale. A filter as indicated by the green circle in Fig. 8(b) with a radius of 26 pixels that allows a resolution of ~0.8μm is used to reconstruct the image. The resulting reconstructed image is shown in Fig. 8(c). Significant cross talk between the zero term and image term prevents the reconstruction of those horizontal bars in the target, which can be seen from the magnified view of the region within the green square in Fig. 8(c), as shown in Fig. 8(j). We then move the reference arm at a speed of ~421μm/s. The resulting hologram is shown in Fig. 8(d). The AS of it is shown in Fig. 8(e), where the center of image term is shifted to the right compared to the Fig. (b). The resulting larger separation between image term and zero term allows the recovery of the horizontal bars by use of a filter with the same size as the in Fig. 8(b), as demonstrated by the reconstruction in Fig. 8(f). However, further increase in filter size causes cross talk noise. To apply a filter size with a radius of 33 pixels that corresponds to the cut off spatial frequency, we increase the speed of the moving reference beam to ~633μm/s. the resulting hologram is shown in Fig. 8(g). The corresponding AS is shown in Fig. 8(h) where a filter with a radius of 33 pixels is allowed without cross talk, which leads to a sharper and diffraction-limited reconstruction as shown in Fig. 8(i) compared to Fig. 8(f), which can be evidenced by comparing the reconstructed scenes bounded by the green squares in Figs. 8(f) and 8(i), magnified views of which are shown in Figs. 8(k) and 8(l) respectively. To summarize, we present a unified theory for off-axis and in-line LCHMs and demonstrate that we are able to change the fringe orientation and density by use of a moving reference beam at different speeds as the wide-field DH can do. This way, we basically identify the LCHM with the off-axis wide-field DH. It is worth noting that, different from wide-filed DH, LCHM is a confocal imaging modality with true optical sectioning.

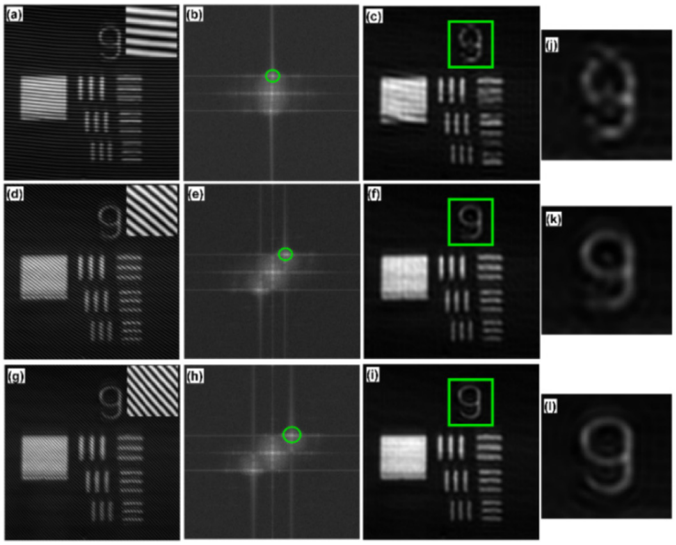

Fig. 8. Demonstration of joint spatiotemporal phase modulation. (a) hologram from off-axis LCHM when the reference beam is static (Inset 3 ×). (b) 2D FT of (a) or 2D AS of (a). (c) Reconstructed intensity from (a). (d) Hologram when reference arm moves at a speed of ~421μm/s. (e) AS. (f) Reconstructed intensity. (g) Hologram when reference arm moves at a speed of ~633μm/s. (h) AS. (i) Reconstructed intensity. (j): Magnified view of the region within the green square in (c). (k): Magnified view of the region within the green square in (f). (l): Magnified view of the region within the green square in (i).

5. Conclusions

In summary, we have presented a high-speed line-scanning confocal holographic microscope which is able to achieve quantitative phase imaging at high frame rate. Using a 20 kHz line scan rate, we achieved a frame rate of 20 Hz for 512x512 pixels en-face confocal images, which is fast enough for in-vivo applications appropriate for LCM [12–16]. The system can be engineered to achieve higher speed if necessary. By using a microscope objective of a NA 0.65, we achieved an axial and lateral resolution of ~3.5 micrometers and ~0.8 micrometers, respectively. By z-stack imaging of a custom silicon target with a stepped structure, we confirmed that the axial sectioning of the LCHM is similar to that of a traditional line-scanning confocal microscope. To realize off-axis holographic detection, we presented two different ways. The first way is using off-axis configuration as traditional off-axis DH does. The second way is introduced by moving the reference arm. Although this method has been applied to SOH and Fourier-Domain optical coherence tomography [11, 19], application of it into the LCHM yields a high-speed *en-face* complex confocal imaging technique. Using a custom axial height phantom fabricated using chrome deposition, we have demonstrated that both off-axis and in-line LCHMs yielded variations in phase corresponding to heights in the ~100 nm range with a contrast-to-noise ratio of ~31 dB. Quantitative confocal phase imaging also enables aberration correction as demonstrated by digitally refocusing an defocused *en-face* confocal image which means other types of optical aberrations in the optical system can also be removed by use of numerical searching [21, 22] or measured phase aberration [18]. For the off-axis LCHM, we are able to measure high-frequency vibration by M-mode, which is beyond reach of the in-line LCHM because of the phase variation introduced the moving reference beam. However, the in-line LCHM decouples the fringe density with the field of view and enjoys higher axial resolution by removing the off-axis optical aberration. Interferometric methods using low spatial coherence light sources have been used to impose confocality in reflectance wide-field imaging systems [23–25]. Incorporation of low spatial coherence sources into the LCHM may enhance the optical sectioning capability. This is the subject of our ongoing research.

Acknowledgments

This work is supported by the National Institutes of Health (NIH) (1R21EB016163-01A1, 1R21HL125125-01A1, 1R01HL118419-01) and the Office of Naval Research (ONR) (MURI N00014-13-1-0649). We would like to thank Prof. M. K. Kim and Dr. D. Clark at University of South Florida for a loan of the phase target.